Simulating polarized Galactic synchrotron emission at all frequencies

the Hammurabi code

A. Waelkens[1],[*] , T. Jaffe[2] , M. Reinecke[1] , F. S. Kitaura[1] , T. A. Enßlin[1]

[1] Max Planck Institut für Astrophysik (MPA), Karl-Schwarzschildstr. 1, 85741 Garching, Germany
  e-mail: waelkens@mpa-garching.mpg.de
[2] Jodrell Bank Centre for Astrophysics, University of Manchester, Alan Turing Building, Oxford Road, Manchester, M13 9PL, UK

ABSTRACT

Context. Galactic synchrotron emission, rotation measure (RM) and the deflection of ultra-high-energy-cosmic-rays (UHECR) permit detailed studies of the Galactic magnetic field (GMF). The synchrotron emission has also to be measured in order to be separated from other astrophysicaly interesting signals like the CMB.
Aims. We present a publicly available code called HAMMURABI for generating mock polarized observations of Galactic synchrotron emission for telescopes like LOFAR, SKA, Planck and WMAP, based on model inputs for the GMF, the cosmic-ray density distribution and the thermal electron density. We also present mock UHECR deflection measure (UDM) maps based on model inputs for the GMF. In future, when UHECR sources are identified, this will allow us to define UDM as a GMF probe in a similar way as polarized radio sources permit us to define rotation measures.
Methods. To demonstrate the code's abilities mock observations are compared to real data as a means to constrain the input parameters of our simulations with a focus on large-scale magnetic field properties.
Results. The Galactic magnetic field models in the literature seem to fail to reproduce any additional observational data which was not included in their design.
Conclusions. As expected, attempts at trying to model the synchrotron, UHECR deflection and RM input parameters, show that any additional observational data set greatly increases the constraints on the models. The HAMMURABI code addresses this by allowing to perform simulations of several different data sets simultaneously, providing the means for a more reliable constraint of the magnetized inter-stellar-medium.

Key words. Radio continuum: ISM – ISM: mangetic fields – ISM: cosmic rays

1. Introduction

There are several different observations which probe the Galactic magnetic field (GMF): synchrotron radiation, rotation measure, UHECR deflection, dust related observations (e.g. starlight polarization Heiles (2000), polarized dust emission), and more recently atom alignment spectroscopic observations were proposed (see Yan & Lazarian 2006).

A better understanding of the inter-stellar magnetized plasma and the radio emission processes related to it is also paramount for current and future CMB experiments (see, e.g., Miville-Deschenes et al. 2008; Page et al. 2007), where in particular measurements of the polarized CMB signal will be limited by our knowledge of foreground emission (Tucci et al. 2005).

Observational studies of the GMF are usually based on one single sort of observable. However, since the different observables and measurement methods provide complementary information, constraining the GMF is logically better if all possible observations are considered simultaneously. We address the need to confront those observations with models by presenting a publicly available software[1] capable of generating mock

synchrotron and Faraday rotation observations as well as mock UHECR deflection maps.

The code is constructed in such a fashion that it should be feasible to adapt it to do any sort of all or partial-sky line-of-sight integral observations, (see, e.g., Waelkens et al. 2008 and Sun et al. 2008).

We will give first a brief account of previous work on GMF modeling in Sect. 2 and then we will give a description of the involved Faraday rotation, UHECR deflection and synchrotron physics, and the simplifying assumptions used in our computation (Sect. 3). The implementation of a line-of-sight (hereafter LOS) integration scheme which mimics the radiative transfer is discussed in Sect. 4. We present some test output using simple standard magnetic field, thermal- and cosmic-ray electron models. We discuss the role of the turbulent field and sub-grid modeling in Sect. 5.1.4, and the one of helical magnetic fields in Sect. 5.1.5. Finally we conclude in Sect. 6.

2. Previous work on Galactic magnetic field modeling

GMF modeling already counts with several contributions from the community. See, e.g., Beuermann et al. (1985); Han et al. (2006); Brown et al. (2003); Haverkorn et al. (2006); Page et al.

---

[*] email: waelkens@mpa-garching.mpg.de
[1] Software available at
http://www.mpa-garching.mpg.de/~waelkens/hammurabi

(2007); Sun et al. (2008) and many others. The data used are mostly a number of total and polarized emission radio surveys of the Galaxy (Taylor et al. 2003; Gaensler et al. 2001; Haslam et al. 1982; Reich & Reich 1986; Page et al. 2007) as well as measurements of Faraday rotation (Dineen & Coles 2005; Johnston-Hollitt et al. 2004; Han et al. 2006) and a starlight polarization catalogue compiled by Heiles (2000). Theoretical predictions are also heavily based on experience obtained from synchrotron observations of other spiral Galaxies (see e.g. Beck et al. 1996). Our work complements previous efforts by making it possible to compare simultaneously the largest possible number of observables to theoretical predictions.

3. Physics included in the code

Here we describe the physical processes included and the assumptions underlying the code.

3.1. Faraday rotation

The polarization angle of an electromagnetic wave is rotated when crossing a magnetized plasma. This effect is known as Faraday rotation (see e.g. Rybicki & Lightman (1979)). The observed polarization angle χ will be a function of the rotation undergone when crossing the magnetized plasma, the square of the observation wavelength and its original (or intrinsic) angle χ_0 at the polarized source,

$$\chi = RM\,\lambda^2 + \chi_0\,. \tag{1}$$

The rotation measure (hereafter RM), which quantifies the linear rate of change of the angle χ as a function of λ^2, is a function of the integral of the magnetic field $\boldsymbol{B}_{LOS}$ along the LOS weighted by the thermal electron density n_e,

$$RM = a_0 \int_{here}^{there} dr\, n_e\, B_{LOS}\,, \tag{2}$$

where $a_0 = q_e^3/(2\pi m_e^2 c^4)$, m_e is the electron mass, c is the speed of light, and q_e is the electron charge.

The RM can be measured directly via a fit to Eq. 1 only in the particular case of a Faraday screen, i.e., if the observer and the polarized source have a cloud of magnetized plasma in between them, but no source-intrinsic Faraday rotation occurs. In the more complicated scenario of several sources along the LOS embedded in the magnetized plasma, the RM cannot be measured in that way since the polarization angle will no longer obey a linear dependence on λ^2. A complicated frequency dependence of the polarization angles arises in such a case, and that is the situation which is typically found in our Galaxy. There, the synchrotron-emitting cosmic-ray electron population is embedded in the magnetized plasma that is producing the Faraday rotation simultaneously.

3.2. Synchrotron emission, total and polarized

Relativistically moving charges in a magnetic field emit synchrotron radiation. In the Galactic case we deal with a cosmic-ray electron population mostly arising from supernova explosions and subsequent shock acceleration, and the GMF of the order of a few micro Gauss with a yet unknown topology. In the following, a couple of simplifying assumptions are made:

 – The relativistic CR electrons have an isotropic velocity distribution, as is measured with high accuracy to be the case at our location in the Galaxy (their propagation, though, is not isotropic due to the presence of ordered magnetic fields; Yan & Lazarian 2008).
 – The cosmic-ray electron spectrum is assumed to be a power law with spectral index p. This widely used simplification is motivated by the theory of shock acceleration (a.k.a. Fermi acceleration, which predicts power law energy distributions; Drury 1983) and is simultaneously confirmed by the measured cosmic-ray electron spectrum at Earth (e.g. Gaisser & Stanev 2004, and references therein). The same observations, as well as sophisticated simulations have, however, shown that the power law assumption is not adequate for the entire energy spectrum (see Strong et al. 2007).

The synchrotron emissivity (i.e. power per unit volume per frequency per solid angle) is partially linearly polarized. Its intensity and polarization properties depend on the strength and orientation of the perpendicular (with respect to the LOS) component of the magnetic field, $B_\perp$, and the cosmic-ray electron spatial and energetic distribution. The emissivities are usually subdivided into two components, $j_{\perp,\parallel} = dE_{\perp,\parallel}/dt\,d\omega\,d\Omega\,dV$, respectively perpendicular and parallel to B_{LOS}, following Rybicki & Lightman (1979) and Westfold (1959):

$$j_\perp(\omega, \boldsymbol{r}) = \frac{1}{4\pi}\frac{\sqrt{3}q^3}{8\pi mc^2}\omega^{\frac{1-p}{2}}\left(\frac{2mc}{3q}\right)^{\frac{1-p}{2}}B_\perp(\boldsymbol{r})^{\frac{p+1}{2}}C(\boldsymbol{r})$$
$$\times\,\Gamma\left(\frac{p}{4}-\frac{1}{12}\right)\left[\frac{2^{\frac{p+1}{2}}}{p+1}\Gamma\left(\frac{p}{4}+\frac{19}{12}\right)+2^{\frac{p-3}{2}}\Gamma\left(\frac{p}{4}+\frac{7}{12}\right)\right], \tag{3}$$

and

$$j_\parallel(\omega, \boldsymbol{r}) = \frac{1}{4\pi}\frac{\sqrt{3}q^3}{8\pi mc^2}\omega^{\frac{1-p}{2}}\left(\frac{2mc}{3q}\right)^{\frac{1-p}{2}}B_\perp(\boldsymbol{r})^{\frac{p+1}{2}}C(\boldsymbol{r})$$
$$\times\,\Gamma\left(\frac{p}{4}-\frac{1}{12}\right)\left[\frac{2^{\frac{p+1}{2}}}{p+1}\Gamma\left(\frac{p}{4}+\frac{19}{12}\right)-2^{\frac{p-3}{2}}\Gamma\left(\frac{p}{4}+\frac{7}{12}\right)\right]. \tag{4}$$

Here C depends on the position in the Galaxy and is defined by $N(\gamma)d\gamma = C\gamma^{-p}d\gamma$, γ being the Lorenz factor, $N(\gamma)$ the number density of electrons $\in [\gamma, \gamma + d\gamma]$, and p is the spectral index as mentioned above. The charge of the electron is given by q_e, the mass by m_e and $\omega = 2\pi\nu$, where ν is the observation frequency. The specific intensity I as a function of observation frequency and LOS direction $\hat{\boldsymbol{n}}$ is

$$I(\omega, \hat{\boldsymbol{n}}) = \int_0^\infty dr\,[j_\perp(\omega, r\hat{\boldsymbol{n}}) + j_\parallel(\omega, r\hat{\boldsymbol{n}})]\,, \tag{5}$$

and the polarized specific intensity P expressed as a complex variable is (see Burn 1966):

$$P(\omega, \hat{\boldsymbol{n}}) = \int_0^\infty dr\,(j_\perp(\omega, r\hat{\boldsymbol{n}}) - j_\parallel(\omega, r\hat{\boldsymbol{n}}))\,e^{-2i\chi(r\hat{\boldsymbol{n}})}.$$

The intrinsic emission polarization angle χ_0 is given by the inclination towards the Galactic North Pole of the local perpendicular-to-the-LOS component of the magnetic field at each position in space (same convention as adopted in Page et al. 2007). The Stokes I, Q, U parameters [2] are then the integrals over solid angle Ω:

$$I = \int d\Omega\,I,$$

---

[2] Here the specific intensities are in italic (*I,Q,U*), while the observed Stokes parameters (I,Q,U) are denoted by Roman letters.

and

$$Q + i\mathrm{U} = \int d\Omega\, P.$$

3.3. UHECR propagation

UHECR's are deflected by the GMF due to the Lorentz force. The Larmour radius for relativistic particles is $r_g = p\,c/Z\,q_e\,B_\perp$, $Z\,q_e$ being the charge of the UHECR, and p the momentum perpendicular to the magnetic field $B_\perp$. Provided, the sources of UHECRs could be identified, an UHECR deflection measure (UDM) can be extracted from the UHECR arrival distribution via fitting the arrival data (position & energy). The net deflection of an UHECR can be approximated by the LOS integral (see e.g. Kachelrieß et al. 2007)

$$\Theta_{\mathrm{offset}} \approx \int dl\, r_g^{-1} = \frac{Z\,q_e}{pc} \int dl B_\perp \equiv \frac{Z\,q_e}{pc} \boldsymbol{UDM}. \tag{6}$$

4. Implementation

In this section we present the implementation of the physics described in Sect. 3.2 and the technical characteristics of the HAMMURABI code. Given a

– 3D GMF model,
– 3D cosmic-ray electron density model,
– 3D thermal electron density model,

HAMMURABI computes full sky maps for

– the Galactic RM contribution to the extra-galactic sources,
– synchrotron I,Q and U Stokes parameters, taking into account intrinsic Galactic Faraday depolarization and,
– UHECR deflection intensity and orientation maps.

The sky maps in HAMMURABI are subdivided into equal area pixels following the HEALPix[3] pixelization scheme of Górski et al. (2005). The total number of pixels for an all-sky map, which defines the angular resolution, is $N_{\mathrm{pix}} = 12\mathrm{NSIDE}^2$, with $\mathrm{NSIDE} = 2^k$ and $k = 0, \ldots, 13$ (a HEALPix package limitation, which can be altered, see App. A). The angular size of a pixel ($\Delta\theta$) can be approximated as

$$\Delta\theta \approx \sqrt{\frac{3}{\pi}} \frac{3600'}{\mathrm{NSIDE}}. \tag{7}$$

The observation volume associated with one of the HEALPix-map pixels is sampled along the LOS at a constant radial interval Δr. As a consequence of the conical shape of the implied effective observation beam, the volume units increase with radius, and hence the weights of the sampling points along the LOS do also increase. To limit the amount of non-homogeneity of the sampling, the code allows the volume resolution to be increased by splitting the beam in sub-beams at some radius, which subsequently can be further split later on. We call the implied 3-D sampling grid the "3D HEALPix grid". See further details in App. A.

Formally, the maximally achievable volume resolution, i.e. the largest volume unit at the finest possible resolution $\Delta\theta \sim 0.43'$, (corresponding to $\mathrm{NSIDE} = 2^{13}$) is $V_{ext} = 4\pi R_{max}^2 \Delta r (12 \cdot 2^{26})^{-1} \sim (4\mathrm{pc})^3$ for $R_{max} \sim 32\mathrm{kpc}$ and $\Delta r = 4\mathrm{pc}$ since we impose an approximately cubic volume unit according to $\Delta r \sim$

---

[3] http://healpix.jpl.nasa.gov

$(4\pi R_{max}^2/12 \cdot 2^{26})^{1/2}$. This implies that variations of the input parameters (magnetic field, thermal electron distribution,...) on scales smaller than this volume can only be taken into account with sub-grid modeling if they persist to the largest radii simulated. Note however that this is an upper limit, given that fluctuations are likely to be stronger closer to the Galactic disk, where resolution, due to the cone-like shape of the observation volume, is going to be higher anyways.

The integration is performed assuming an optically thin medium. Sun et al. (2008) enhanced the code by introducing free-free absorption. This implementation, relevant mainly at frequencies below a GHz, is present in the code but not described here. Furthermore, Sun et al. (2008) also introduced a coupling between the thermal electron density and the random component of the RM. This implementation is necessary to explain the degree of depolarization at their simulated 1.4GHz map. It is also present in the code but not described here. For further details see Sun et al. (2008).

The 3D HEALPix grid, since the value of one observation pixel stems from the contribution of several sub-beams, allows one approximately to take into account effects like beam depolarization. See App. A.1 for details.

4.1. Features

HAMMURABI is also suited for simulations of partial sky coverage. A single pixel or a list of pixels representing either patches or separate locations on the sky output maps can be computed. An extension to that is the option to compute RMs for an individual pixel only up to a certain specified distance. This is relevant for simulating RM observations of radio pulsars or other polarized sources with distance information in our own Galaxy. Polarized sources along the same LOS allow us to probe fractions of the ISM plasma, unlike extra-galactic polarized sources which give us the integrated RM along the entire LOS through the Galaxy. The mock observations for this case are done without beam-splitting and at highest possible angular resolution, since RM are effectively obtained from point sources.

5. Examples

In this section we choose standard 3D input models for a demonstration of the code's results. It is not the scope of this work to present new scientific findings, but to present a proof of concept of what can be done with HAMMURABI. An actual application of the code has been done in Sun et al. (2008), and we will briefly refer to some of their results here. Their preferred GMF model and cosmic-ray electron model, derived by trying to fit a broad range of observables, are compared to the corresponding models suggested by Page et al. (2007), fitted to reproduce solely the polarization angles observed by the WMAP satellite. Note that it has been shown by Sun et al. (2008) that the Page et al. (2007) model, as well as every model from the literature analyzed in their work, fail to reproduce different sorts of observations of the magnetized ISM satisfactorily, since they are all constructed by considering only a particular sort of data. The discrepancies of the models presented here, visible by eye, are suitable for displaying the codes abilities.

5.1. Inputs

5.1.1. The thermal electron density model

For the thermal electron distribution we use the NE2001 model (see Cordes & Lazio 2002). This model subdivides the Galaxy into several large-scale structure elements like a thin disk, a thick disk, spiral arms, as well as some local small-scale elements such as supernova bubbles.

5.1.2. The cosmic-ray electron density model

We use the cosmic-ray electron density models suggested by Page et al. (2007) and Sun et al. (2008).

– The model in Page et al. (2007) consists of an exponentially decaying disc with characteristic hight $h_d = 1$ kpc and a characteristic radius of $h_r = 5$ kpc. Note that to compute the synchrotron emissivity, as can be seen in Eqs. 3 and 4, we need the spatially dependent function C, not the cosmic-ray electron density. However, since we are assuming a Galaxy-wide unique power-law energy spectral slope with a spectral index $p = 3$ (note that in principle the code allows to associate a different spectral index for each volume unit), these quantities are proportional to each other. The value of $C_{\text{Earth}} = 6.4 \cdot 10^{-5} \text{cm}^{-3}$ at Earth's position is observed (see e.g. Fig. 4 of Strong et al. 2007), and although it is not clear that it is representative for other regions in the Galaxy (Sun et al. 2008; Pohl & Esposito 1998; Strong et al. 2004), we use it as a zeroth order approximation for the normalization (which is not necessary/provided in Page et al. (2007)) of our distribution,

$$C = C_0 \, exp \left[-r/h_r \right] \, sech^2(z/h_d) . \tag{8}$$

Here r is the Galactic radius, while z is the hight. C_0 is such that $C = C_{\text{Earth}}$ at Earths position.

– Sun et al. (2008) proposes

$$C(R, z) = C_0 \exp \left(-\frac{R - R_\odot}{8 \text{ kpc}} - \frac{|z|}{1 \text{ kpc}} \right) \tag{9}$$

with $C_0 = C_{\text{Earth}}$, while $C(R < 3 \text{ kpc}) = C(R = 3 \text{ kpc})$ and $C(|z| > 1) = 0$. The abrupt truncation at a scale hight of $|z| > 1$ as discussed by Sun et al. (2008) is necessary to acomodate a low synchrotron emission at high latitudes where an anomalously strong halo magnetic field is required to account for high RM measurements. Sun et al. (2008) warn that this seems unrealistic and suggests that a larger scale hight of the thermal electron density could resolve the problem by diminishing the required value of the halo magnetic field. They conclude that the high-latitude thermal electron density should be better investigated. Furthermore the spectral index p is 3 for observation frequencies larger than 408 MHz and 2 otherwise. Sun et al. (2008) adopt this simplification based on observations of Roger et al. (1999) and Reich & Reich (1988a,b), which support a flatter spectrum below 408 MHz.

As mentioned in Sect. 3.2, simulations (see the GALPROP code by Strong et al. 2007) show that the assumption of a power-law energy distribution is not applicable to the entire spectrum. The same simulations also present a seizably more sophisticated cosmic-ray electron distribution. Incorporating the output of those simulations into HAMMURABI is planned as an extension.

5.1.3. Large-scale Galactic magnetic field models

The behavior of the synchrotron emissivity is mainly driven by the magnetic field distribution, as shown in Eqs. 3 and 4.

It is a common practice to subdivide the Galactic magnetic field in a large-scale and a small-scale component. The latter will be addressed in the next section 5.1.4. The subdivision in these two classes of fields is somewhat arbitrary, and we adopt here the convention that the large-scale field is statistically anisotropic at any point in the galaxy, while the small-scale field is not.

GMF modeling has been done in direct studies of the galactic magnetic field. See Page et al. (2007); Sun et al. (2008); Jansson et al. (2007); Haverkorn et al. (2006); Brown et al. (2003); Han et al. (2006), and others. In the context of UHECR propagation (see Kachelrieß et al. 2007; Tinyakov & Tkachev 2002; Prouza & Šmída 2003; Harari et al. 2000). Typically GMF models, inspired by observations of the radio-polarization patterns of other spiral galaxies, present spiral-like structures. Here we present simulations using the model from Page et al. (2007) and the favored (ASS+RING) model proposed by Sun et al. (2008). The expressions are reproduced in the App. B. Further magnetic field models can easily be incorporated in the code.

5.1.4. Small-scale magnetic field

Although the turbulent component of the GMF has been studied extensively (see e.g. Haverkorn et al. 2003; Han et al. 2004; Haverkorn et al. 2006, 2008) there is, to our knowledge, not yet any model which describes it to a satisfactory degree. Observational constraints on its relative strength compared to that of the large-scale field put it at roughly the same amplitude (i.e. a couple of micro Gauss; Beck 2001). HAMMURABI allows one to simulate, given a magnetic field power spectrum, a Gaussian random field realization. A realistic turbulent field, however, needs not be Gaussian, since simulations of turbulence show sheet like structures evidently different from what is expected from a Gaussian field (see e.g. Schekochihin et al. 2004; Schekochihin & Cowley 2006). This means that the Gaussian random field should per construction reproduce the correct two point statistics of a real field, however it will probably not reproduce higher order statistics as real fields are not observed to be Gaussian (see e.g. the figures in Jaegers 1987; Clarke & Ensslin 2006). Furthermore, this modeling assumes the power spectrum of the field to be known, which in the case of the Galaxy, to our knowledge, has not yet been determined. There are, however, measurements of the magnetic power spectrum in the intra-cluster medium (e.g. Vogt & Enßlin 2005; Guidetti et al. 2008; Govoni et al. 2006).

5.1.5. Helical fields

Helical magnetic fields have a broken mirror symmetry and can best be visualized by twisted flux tubes. Topological helicity is given by $\int dV \, A \cdot B$, where A is the vector potential of the field, $B = \nabla \times A$. Current helicity is given by $\int dV \, j \cdot B$, where j is the electrical current, satisfying $j = \nabla \times B$. Both types of helicity are closely related. Topological helicity is a nearly conserved quantity, even in non-ideal MHD, and plays a crucial role in magnetic dynamo theory. Therefore HAMMURABI was adapted to read in random small-scale fields with magnetic helicity generated by a separate code. This code, also available for download, is called GARFIELDS (first applied in Kitaura & Ensslin 2007), where helic-

ity is imprinted onto a divergence free Gaussian random field $\boldsymbol{B'}$ by

$$\hat{B}_m = \frac{1}{\sqrt{1+\alpha^2}} \left(\delta_{jm} + i\alpha\epsilon_{ijm}\overline{k}_i \right) \hat{B}'_j. \tag{10}$$

Here $\hat{B}'_i = \hat{B}'_i(\boldsymbol{k})$ and it is such that $\langle \hat{B}'_i \hat{B}'^*_j \rangle = \left(\delta_{ij} - \overline{k}_i\overline{k}_j \right) P(k)/2$, where $P(k)$ is the magnetic power spectrum. The hat denotes a Fourier transform, δ is the Kronecker delta, $\overline{k}_i$ is an unit vector and ϵ_{ijk} is the permutation symbol. Maximal helicity is found for $\alpha = -1$ and 1. This leads to a magnetic correlation tensor of the form

$$\langle \hat{B}_i \hat{B}^*_j \rangle = \left[\frac{1}{2} \left(\delta_{ij} - \overline{k}_i\overline{k}_j \right) - i\epsilon_{ijk}\overline{k}_k \frac{\alpha}{1+\alpha^2} \right] P(k). \tag{11}$$

5.2. Synchrotron and RM outputs: comparison with observations

In this section we compare our example simulation with observed data. The mock total intensity I, polarized intensity P, polarization angle PA and RM maps for our two different field configurations and slightly different cosmic-ray electron distributions of Sun et al. (2008) and Page et al. (2007) are shown in comparison to the observed synchrotron emission at 0.408 MHz (total intensity) and 23 GHz (polarized emission), and a RM map extrapolated from the existing still sparse RM observations (Fig. 1). All maps in this figure and throughout the paper are at a resolution of NSIDE = 128, $\Delta r = 0.21$kpc, $H_{obs} = 2$, $H_{max} = 3$ (see definitions in App. A). A Gaussian random field with a Kolmogorov spectrum $k^{-5/3}$ with a lower cutoff at $k_0 = 1$kpc^{-1} (see, e.g., Han et al. 2004), and an upper cutoff given by the Nyquist frequency of the simulation box $k_{Nyquist} = 3.2$kpc^{-1}, was added on both large-scale GMF models. We caution that this scale range is insufficient to describe the turbulent field in the Galaxy, as can be seen when noticing the even smaller-scale fluctuations present only in the observations, however it serves our demonstration purposes. Following Sun et al. (2008) the random field amplitude is $\langle B^2_{ran} \rangle^{1/2} = 3\mu$G.

Magnetic field models in the literature are mostly designed to fit a selected set of data. For example Page et al. (2007) fit PA observations, and, as can be seen in Fig. 1, does this remarkably well. However, their model evidently fails to reproduce any of the other observations (as shown by Sun et al. 2008). Furthermore Sun et al. (2008) note that most spiral magnetic field configurations have rather similar PA, suggesting a highly degenerate fitting problem.

The Sun et al. (2008) models for the GMF and the cosmic-ray electron distribution were designed to fit longitude and latitude RM profile observations and I and P observations at 408 MHz, 1.4 GHz and 22.8 GHz, but no optimization was performed for the PA observations. Note also that Sun et al. (2008), unlike Page et al. (2007), who did a parameter scan, adjust the model parameters based on trial and error. The attentive reader might notice a faint horizontal stripe like pattern seen in the I and P simulations of this model, which is due to a combination of our limited radial step size $\Delta r = 0.21$kpc, and the abrupt cut of the cosmic-ray electron density at 1 kpc away from the Galactic plane (as discussed in Sec. 5.1.2). In other words, the code cannot resolve a sharp cut. A smaller Δr, of course, makes the feature vanish, though it would be inconsistent with our recommendation in App. A to peg Δr to the NSIDE parameter. Probably the most striking difference between the two models lies in the different RM maps, mainly due to so called field reversals in the Sun et al. (2008) model, which are absent in the WMAP model.
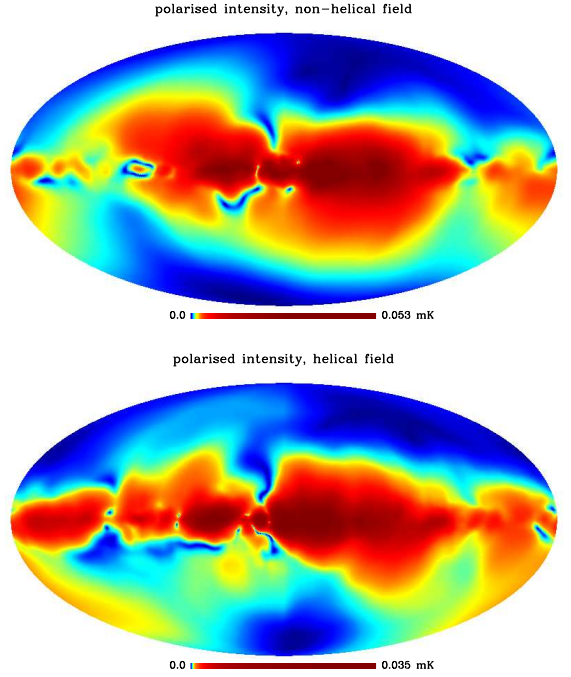

Fig. 2. Polarized intensity of a field without and one with helicity. The colors in the plot are equally distributed over area to enhance the visualization of structures at the expense of proportionality information.

5.3. Helicity in the ISM?

Our code provides the possibility to study the effects of magnetic helicity on observations. In Fig. 2 a field realization with and without helicity are compared. Although they are clearly different, there is no qualitative difference between the single frequency maps from fields with helicity and without. These results reinforce that measuring helicity in the ISM is difficult and the necessary multi frequency methods to extract it e.g. from Faraday tomography observations (Brentjens & de Bruyn 2005; Schnitzeler et al. 2007) still have to be developed. The availability of a tool for generating mock observations might be of assistance for the development of such methods and for feasibility studies of observations aiming at determining the helicity in the ISM.

5.4. UHECR deflection outputs

HAMMURABI as a generic tool to study the GMF also helps to prepare for UHECR-based magnetic field studies, once the sources of the UHECR particles are identified. We included the option to compute the deflection of ultra-relativistic charges by the GMF in the code. This is yet another observable by which the GMF may be further constrained in the future. Presently there are only a couple of hundred registered events and their origin is still speculative (The Pierre Auger Collaboration et al. 2007). Fig. 3 represents the deflection intensity for the large-scale Sun et al. (2008) model. Note that the strong halo field is controversial (as discussed in Sect. 5.1.2). The deflection angle of an individual UHECR is obtained by multiplying the deflection intensity map with $Z q_e/p c$ of this particle, as in Eq. 6.
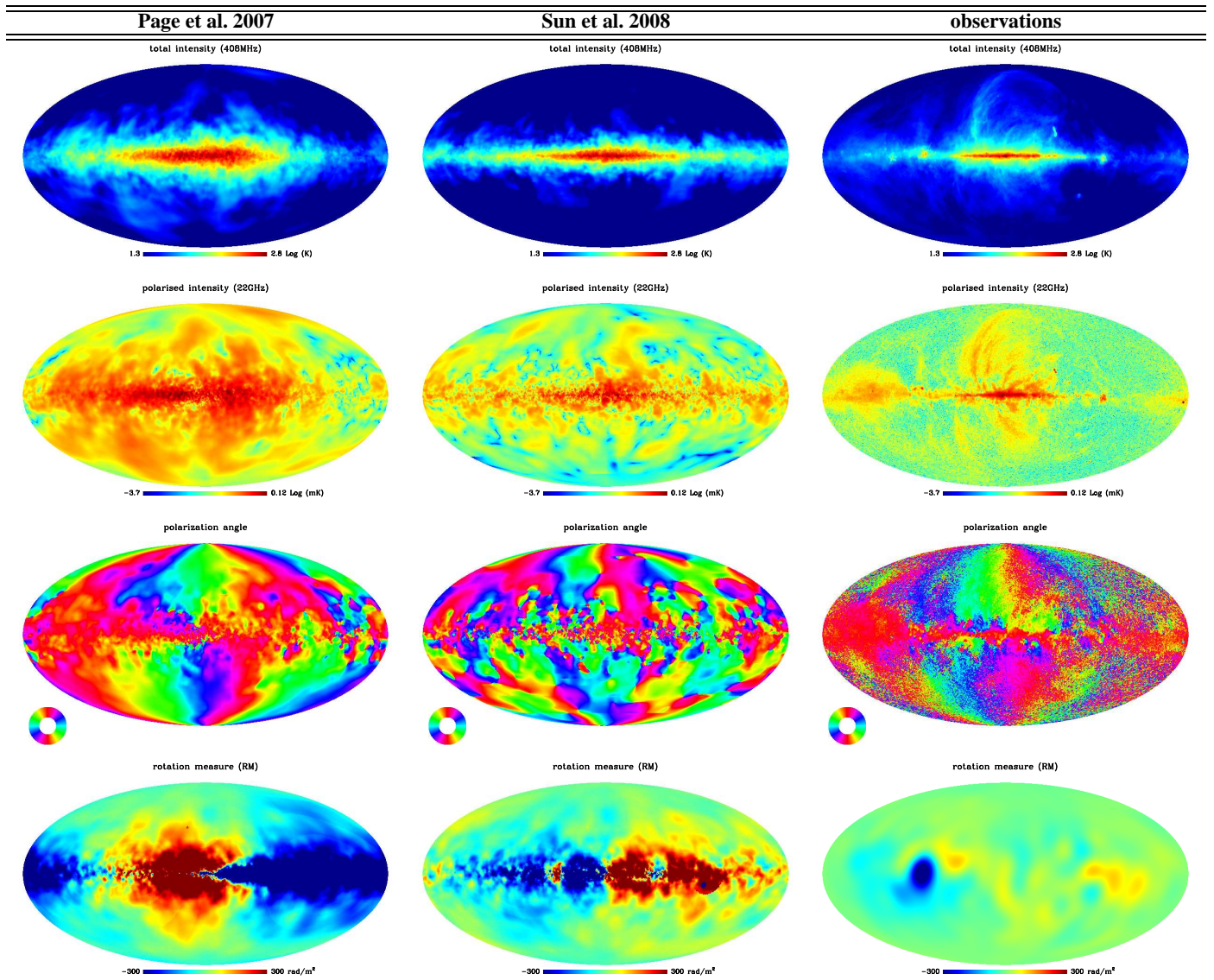
Fig. 1. Comparison of mock observations based on models from Page et al. (2007) and Sun et al. (2008) with observed data. Each row is respectively total intensity I, polarized intensity P, polarization angle PA and rotation measure RM. The third column contains the observables. I is from Haslam et al. (1981, 1982), P and PA are WMAP observations (Page et al. 2007; Hinshaw et al. 2008) , while the RM is from Dineen & Coles (2005) using the Simard-Normandin et al. (1981) data.
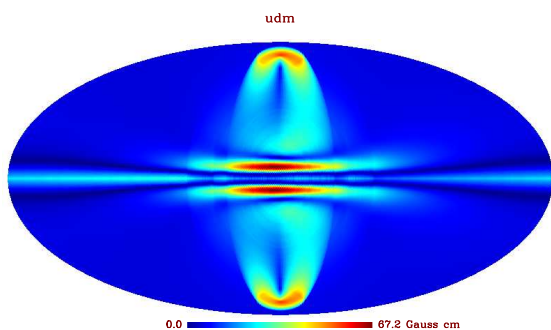

Fig. 3. UHECR deflection measure map from the Sun et al. (2008) large-scale magnetic field model. Currently only a couple of hundred UHECR detections have been reported.

5.4.1. A LOFAR, SKA, WMAP, Planck tool

The frequency range of ʜᴀᴍᴍᴜʀᴀʙɪ synchrotron simulations, from ~ 100 MHz up to ~ 100 GHz, covers currently running experiments like WMAP as well as the upcoming generation of radio telescopes: Planck, LOFAR, SKA and the like. ʜᴀᴍᴍᴜʀᴀʙɪ has been developed to support the scientific exploitation of the data of these experiments and to provide synthetic observations for design studies. It is capable of generating full- or partial-sky (not shown) maps as well as individual LOS (see Figure 5), which are useful for non diffuse measurements, e.g. RMs.

Figure 4 shows the full sky polarized intensity P for the aforementioned Sun et al. (2008) model (applying their low frequency corrections and coupling between thermal electrons and the random RM component).

In principle, multi-frequency simulations permit one to take into account beam-width depolarization effects. Since the measurements of real telescopes correspond to an integral over some frequency band, band-width depolarization will also happen provided the Faraday effects are strong enough across the band-width. Although band-width depolarization is not a stan-
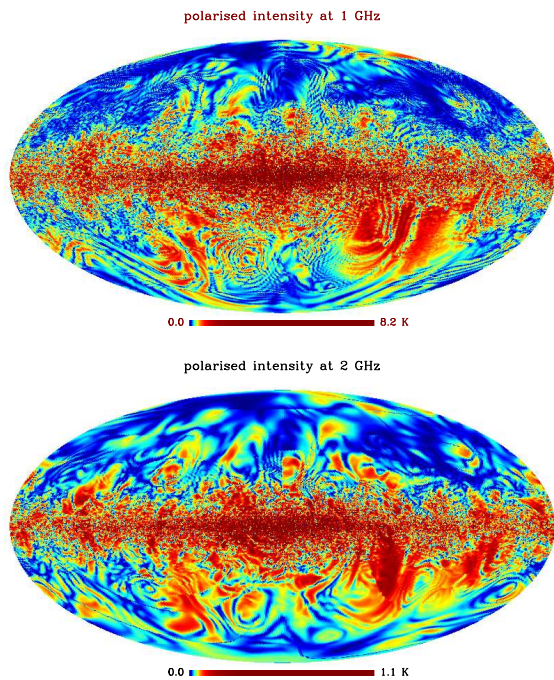
polarised intensity at 1 GHz

0.0   8.2 K

polarised intensity at 2 GHz

0.0   1.1 K

Fig. 4. Simulated polarized intensity P at 1 and at 2GHz of the Sun et al. (2008) model. The colors in the plot are equally distributed over area to enhance the visualization of structures at the expense of proportionality information. The Faraday depolarization effect changes the complex patterns as a function of the wavelength. The higher thermal electron density on the Galactic plane keeps Faraday depolarization active long after it already ceased to be relevant in the Galactic halo.
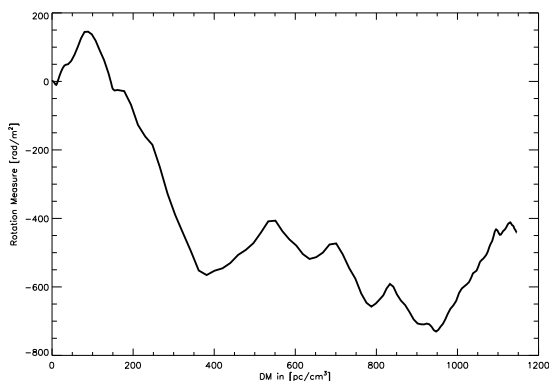
Fig. 5. The simulated rotation measure as a function of dispersion measure. Here we used a Gaussian random field with an upper cutoff of 5 kpc and a root-mean-square of 6 μGauss. Pulsar polarization measurements are, with the advent of SKA, expected to become very numerous, allowing us to chart the GMF in three-dimensions, as is shown in the present plot.

dard HAMMURABI feature, it can be emulated by coadding closely spaced frequency maps.

The framework of the code is built to allow additions of any other beam-like observables such as in Waelkens et al. (2008), Sun et al. (2008).

6. Conclusion

We have presented the HAMMURABI code, a tool for simulating rotation measure maps, total and polarized Galactic syn-

chrotron emission maps taking into account Faraday rotational-depolarization effects, as well as UHECR deflection maps.

Drawing a set of well known input models from the literature (NE2001 for the thermal electron distribution, Sun et al. (2008) and Page et al. (2007) for the cosmic-ray electron distribution and the Galactic magnetic field), we show example outputs comparing them to corresponding observations to illustrate the code's abilities as a scientific tool for charting the Galactic magnetized plasma and the cosmic-ray electron distribution.

Full galaxy simulations are currently limited by the finite HEALPix-grid resolution, thus being unable to probe fluctuations with characteristic lengths of less than 4pc. A second caveat is that the widely used approximation of a power-law energy distribution of the cosmic-ray electrons has been shown to be questionable by sophisticated cosmic ray propagation simulations (Strong et al. 2007). The degree to which this affects the precision of our simulations has yet to be assessed. Furthermore, our non-ray-tracing calculations of UHECR deflections might not fulfill strict precision requirements as soon as the UHECR's trajectory through the Galaxy is significantly bent; they serve rather as a first approximation.

It was shown that, unsurprisingly, models designed to fit only a fraction of the available observational data on GMF might fail to reproduce the remaining observational information not taken into account in their construction.

This is an indication that the constraints to the GMF might be highly degenerate. Hence confronting the models with the broadest possible range of observations on the Galactic magnetic field is paramount to achieving any useful statement about the field.

Furthermore we have displayed HAMMURABI's capabilities of generating low-frequency mock observations, where Faraday effects play a significant role. This can be used for feasibility studies and the analysis of the actual observations of forth coming low-frequency radio telescopes like LOFAR or the SKA (note that the latter can also observe at high-frequencies).

HAMMURABI can be applied for constraining the Galactic magnetized plasma and increasing our understanding on radio Galactic emission and UHECR source locations. Already a worthy scientific goal by itself, it will also have implications on our understanding on foreground emission subtraction for experiments like Planck or WMAP.

References

Beck, R. 2001, Space Science Reviews, 99, 243
Beck, R., Brandenburg, A., Moss, D., Shukurov, A., & Sokoloff, D. 1996, ARA&A, 34, 155
Beuermann, K., Kanbach, G., & Berkhuijsen, E. M. 1985, A&A, 153, 17
Brentjens, M. A. & de Bruyn, A. G. 2005, A&A, 441, 1217
Brown, J. C., Taylor, A. R., Wielebinski, R., & Mueller, P. 2003, ApJ, 592, L29
Burn, B. J. 1966, MNRAS, 133, 67
Clarke, T. E. & Ensslin, T. A. 2006, AJ, 131, 2900
Cordes, J. M. & Lazio, T. J. W. 2002, ArXiv Astrophysics e-prints
Dineen, P. & Coles, P. 2005, MNRAS, 362, 403
Drury, L. O. 1983, Reports of Progress in Physics, 46, 973

Gaensler, B. M., Dickey, J. M., McClure-Griffiths, N. M., et al. 2001, ApJ, 549, 959

Gaisser, T. K. & Stanev, T. 2004, Physics Letters B, 592, 228

Górski, K. M., Hivon, E., Banday, A. J., et al. 2005, ApJ, 622, 759

Govoni, F., Murgia, M., Feretti, L., et al. 2006, A&A, 460, 425

Guidetti, D., Murgia, M., Govoni, F., et al. 2008, A&A, 483, 699

Han, J. L., Ferriere, K., & Manchester, R. N. 2004, ApJ, 610, 820

Han, J. L., Manchester, R. N., Lyne, A. G., Qiao, G. J., & van Straten, W. 2006, ApJ, 642, 868

Harari, D., Mollerach, S., & Roulet, E. 2000, Journal of High Energy Physics, 2, 35

Haslam, C. G. T., Klein, U., Salter, C. J., et al. 1981, A&A, 100, 209

Haslam, C. G. T., Salter, C. J., Stoffel, H., & Wilson, W. E. 1982, A&AS, 47, 1

Haverkorn, M., Brown, J. C., Gaensler, B. M., & McClure-Griffiths, N. M. 2008, ArXiv e-prints, 802

Haverkorn, M., Gaensler, B. M., Brown, J. C., et al. 2006, ApJ, 637, L33

Haverkorn, M., Katgert, P., & de Bruyn, A. G. 2003, A&A, 403, 1045

Heiles, C. 2000, AJ, 119, 923

Hinshaw, G., Weiland, J. L., Hill, R. S., et al. 2008, ArXiv e-prints, 803

Jaegers, W. J. 1987, A&AS, 71, 603

Jansson, R., Farrar, G. R., Waelkens, A., & Enßlin, T. A. 2007, ArXiv e-prints, 708

Johnston-Hollitt, M., Hollitt, C. P., & Ekers, R. D. 2004, in The Magnetized Interstellar Medium, 13–18

Kachelrieß, M., Serpico, P. D., & Teshima, M. 2007, Astroparticle Physics, 26, 378

Kitaura, F. S. & Ensslin, T. A. 2007, ArXiv e-prints, 705

Miville-Deschenes, M. ., Ysard, N., Lavabre, A., et al. 2008, ArXiv e-prints, 802

Page, L., Hinshaw, G., Komatsu, E., et al. 2007, ApJS, 170, 335

Pohl, M. & Esposito, J. A. 1998, ApJ, 507, 327

Prouza, M. & Šmída, R. 2003, A&A, 410, 1

Reich, P. & Reich, W. 1986, A&AS, 63, 205

Reich, P. & Reich, W. 1988a, A&AS, 74, 7

Reich, P. & Reich, W. 1988b, A&A, 196, 211

Roger, R. S., Costain, C. H., Landecker, T. L., & Swerdlyk, C. M. 1999, A&AS, 137, 7

Rybicki, G. B. & Lightman, A. P. 1979, Radiative processes in astrophysics (New York, Wiley-Interscience, 1979.)

Schekochihin, A. A. & Cowley, S. C. 2006, Physics of Plasmas, 13, 056501

Schekochihin, A. A., Cowley, S. C., Taylor, S. F., Maron, J. L., & McWilliams, J. C. 2004, ApJ, 612, 276

Schnitzeler, D. H. F. M., Katgert, P., & de Bruyn, A. G. 2007, A&A, 471, L21

Simard-Normandin, M., Kronberg, P. P., & Button, S. 1981, ApJS, 45, 97

Strong, A. W., Moskalenko, I. V., & Ptuskin, V. S. 2007, Annual Review of Nuclear and Particle Science, 57, 285

Strong, A. W., Moskalenko, I. V., & Reimer, O. 2004, ApJ, 613, 962

Sun, X. H., Reich, W., Waelkens, A., & Enßlin, T. A. 2008, A&A, 477, 573

Taylor, A. R., Gibson, S. J., Peracaula, M., et al. 2003, AJ, 125, 3145

The Pierre Auger Collaboration, Abraham, J., Abreu, P., et al. 2007, Science, 318, 938

Tinyakov, P. G. & Tkachev, I. I. 2002, Astroparticle Physics, 18, 165

Tucci, M., Martínez-González, E., Vielva, P., & Delabrouille, J. 2005, MNRAS, 360, 935

Vogt, C. & Enßlin, T. A. 2005, A&A, 434, 67

Waelkens, A., Maturi, M., & Enßlin, T. A. 2008, MNRAS, 383, 1425

Westfold, K. C. 1959, ApJ, 130, 241

Yan, H. & Lazarian, A. 2006, ApJ, 653, 1292

Yan, H. & Lazarian, A. 2008, ApJ, 673, 942

Appendix A: The 3D HEALPix grid

The ʜᴀᴍᴍᴜʀᴀʙɪ code generates HEALPix maps with an angular resolution defined by the parameter NSIDE = 2^k, where $k \in [0, 13]$ (the maximum k is a computational limit; it could be extended only by alterations to the original HEALPix package). The integration volume has a cone-like geometry. To minimize the non-homogeneous volume sampling induced by that, the integration volume is consecutively subdivided in so-called sub-beams. Each section of these sub-beams is contained in a shell centered on Earth. We shall call this grid the 3D HEALPix grid.

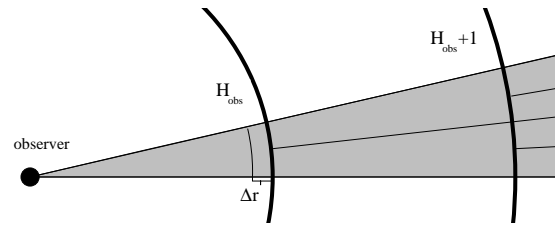This subdivision will depend on

Fig. A.1. An example of the 3D HEALPix grid. For simplicity it is presented in 2D. The gray shaded area corresponds to the integration volume.

- the radial length Δr of each volume unit in the observation beam,
- how many shells $H_{\max}$ in total there will be,
- what resolution, or equivalently what $\mathrm{NSIDE}_{\mathrm{obs}}$ the observation shell has,
- and finally the shell number of the observation shell H_{obs}.

See an example in Fig. A.1.

The distances at which the beam is split, or equivalently the upper boundaries [4] of the shells, are given by

$$d_i = R_{max}2^{i-H_{\max}}. \tag{A.1}$$

Where the index $i \in [1, H_{\max}]$. Due to the disc-like shape of our galaxy, the effective radius out to which we perform our computations varies and decreases sharply towards high latitudes and towards the anti-center direction.

The maximum volume for each shell is a constant corresponding approximately to

$$V_{max} = 4\pi d_{H_{\mathrm{obs}}}^2 \frac{\Delta r}{12 \cdot \mathrm{NSIDE}_{\mathrm{obs}}^2}. \tag{A.2}$$

We suggest [5] a definition of Δr such that the maximum volume unit at the largest shell is close to a cubic form.

Note that the maximum volume unit V_{max} decreases with higher observation resolution. It defines the minimum scale which can be resolved with the code for a certain resolution. Fluctuations smaller than that cannot be resolved by the code. This is a formal upper limit, since the Galactic regions more prone to have small scale fluctuations are likely not at the far end of the observation volume, where V_{max} is located, but instead at regions closer to the observer, where the spatial resolution is finer.

A.1. Line of sight integration

For the i-th volume element of a cone, according to the formulae in the theoretical section 3, we compute the following,

$$
\begin{cases}
I_i^{\mathrm{syn}} &= C_I B_{i,\,\perp}^{(1-p)/2} \nu^{(1+p)/2} \Delta r \\
P_i &= C_P B_{i,\,\perp}^{(1-p)/2} \nu^{(1+p)/2} \Delta r \\
RM_i &= a_0 n_{e\,i} B_{i,\,LOS} \Delta r \\
\chi_i &= \sum_{j=1}^{i} RM_j \lambda^2 + \chi_{i,\,0} \\
Q_i &= P_i \cos(2\chi_i) \\
U_i &= P_i \sin(2\chi_i) \\
B_{x,\,i} &= B_i \cos(\chi_{i,\,0}) \\
B_{y,\,i} &= B_i \sin(\chi_{i,\,0})
\end{cases}
\tag{A.3}
$$

---

[4] The code will automatically round down d_i to a multiple of Δr.

[5] Choices of any other constant are of course possible.

Note that the calculated Stokes values U_i and Q_i for each volume element include the effect of foreground RM. The CR electrons are assumed to follow a power law with an energy spectral index p (see Sect. 3.2). The values C_I and C_P are dependent on the spatialy dependent spectral index p and the spatial distribution component of the cosmic rays C, and can be obtained from the formulae given in section 3 and Rybicki & Lightman (1979). The intrinsic polarization angle $\chi_{i,0}$ is locally defined as zero if the magnetic field is pointing in positive Galactic-coordinates l-direction and $\pi/2$ when the magnetic field is pointing in positive Galactic-coordinates b-direction.

The intensities, RMs and UDMs for a pixel are straightforward to compute. They consist of an integral of the contributions from all the volume units as below (Eq. A.4). For the intensities, in case of a subdivision of the observation cone into sub-cones, the computation is done by averaging the set of sub-cones. This, however, is not done for the UDM and RM values, since they are respectively observed as being linearly dependent on λ^3 and λ^2, where λ is the wavelength. The beam averaging could destroy that linear behavior [6]. The UHECR deflection measure is given by $UDM = \sqrt{UDM_x^2 + UDM_y^2}$, while the deflection orientation is given by $\Theta_{\text{defl}} = \arctan \frac{UDM_x}{UDM_y}$.

$$
\left\{
\begin{array}{rcl}
I & = & \sum_i I_i \\
Q & = & \sum_i Q_i \\
U & = & \sum_i U_i \\
RM & = & \sum_i RM_i \\
UDM_x & = & \sum_i B_{x,i} \Delta r \\
UDM_y & = & \sum_i B_{x,i} \Delta r
\end{array}
\right.
\tag{A.4}
$$

Appendix B: Magnetic field models

For the convenience of the reader we present the parameterizations of the galactic magnetic field folowing Page et al. (2007) and Sun et al. (2008). Everything is in the usual cylindrical coordinates, whose origin lies at the Galactic center. The x-axis of the coordinate system points in the opposite direction of the Sun, while the z-axis points towards the Galactic north.

– Page et al. (2007) writes

$$
\boldsymbol{B}(r, \phi, z) = B_0 \left[\cos \psi(r) \cos \chi(z) \hat{r} + \right.
\tag{B.1}
$$
$$
\left. \sin \psi(r) \cos \chi(z) \hat{\phi} + \sin \chi(z) \hat{z} \right]
\tag{B.2}
$$

Here $\psi(r) = \psi_0 + \psi_1 ln(r/8\text{kpc})$, $\chi(z) = \chi_0 \tanh(z/1\text{kpc})$. The radial variable $r \in [3\text{kpc}, 8\text{kpc}]$, $\chi_0 = 25^\text{o}$, $\psi_1 = 0.9^\text{o}$ and $\psi_0 = 27^\text{o}$. B_0 is not specified in Page et al. (2007) and we put $B_0 = 4\,\mu G$.
– While Sun et al. (2008) presents some suggestions for fields, and we pick their *ASS+RING* parameterization:

$$
\left\{
\begin{array}{rcl}
B_{\hat{r}}^D & = & D_1(R, \phi, z) D_2(R, \phi, z) \sin p \\
B_{\hat{\phi}}^D & = & -D_1(R, \phi, z) D_2(R, \phi, z) \cos p \\
B_{\hat{z}}^D & = & 0
\end{array}
\right.
\tag{B.3}
$$

Where

$$
D_1(r, z) = \left\{
\begin{array}{ll}
B_0 \exp\left(-\dfrac{r - R_\odot}{R_0} - \dfrac{|z|}{z_0}\right) & r > R_c \\
B_c & r \leq R_c
\end{array}
\right.
\tag{B.4}
$$

Here $R_0 = 10$ kpc, $z_0 = 1$ kpc, $R_c = 5$ kpc, $B_0 = 2\,\mu G$ and $B_c = 2\,\mu G$. and

$$
D_2(r) = \left\{
\begin{array}{ll}
+1 & r > 7.5 \text{ kpc} \\
-1 & 6 \text{ kpc} < r \leq 7.5 \text{ kpc} \\
+1 & 5 \text{ kpc} < r \leq 6 \text{ kpc} \\
-1 & r \leq 5 \text{ kpc}
\end{array}
\right.
\tag{B.5}
$$

While the halo field is given by

$$
B_\phi^H(r, z) = B_0^H \frac{1}{1 + \left(\dfrac{|z| - z_0^H}{z_1^H}\right)^2} \frac{r}{R_0^H} \exp\left(-\frac{r - R_0^H}{R_0^H}\right)
\tag{B.6}
$$

and the parameters are $z_0^H = 1.5$ kpc, $B_0^H = 10\,\mu G$, $R_0^H = 4$ kpc, $z_1^H = 0.2$ kpc (for $|z| < z_0^H$), and $z_1^H = 0.4$ kpc (otherwise).

---

[6] The final RM and UDM value is defined as the sum of the highest possible resolution sub-beam to all parent beam contributions. Thus one intensity pixel might have several corresponding RM and UDM pixels, since those are computed for higher resolutions, while the former averages over the same higher resolution computations.